

# Characterization of deformable mirrors for spherical aberration correction in optical sectioning microscopy

Michael Shaw,<sup>1,\*</sup> Simon Hall,<sup>1</sup> Steven Knox,<sup>1</sup> Richard Stevens<sup>1</sup> and Carl Paterson,<sup>2</sup>

<sup>1</sup>National Physical Laboratory, Hampton Road, Teddington, Middlesex, TW11 0LW, UK

<sup>2</sup>Photonics Group, The Blackett Laboratory, Imperial College, London SW7 2BW, UK

\*mike.shaw@npl.co.uk

**Abstract:** In this paper we describe the wavefront aberrations that arise when imaging biological specimens using an optical sectioning microscope and generate simulated wavefronts for a planar refractive index mismatch. We then investigate the capability of two deformable mirrors for correcting spherical aberration at different focusing depths for three different microscope objective lenses. Along with measurement and analysis of the mirror influence functions we determine the optimum mirror pupil size and number of spatial modes included in the wavefront expansion and we present measurements of actuator linearity and hysteresis. We find that both mirrors are capable of correcting the wavefront aberration to improve imaging and greatly extend the depth at which diffraction limited imaging is possible.

©2010 Optical Society of America

**OCIS codes:** (110.1080) Active or adaptive optics; (110.0180) Microscopy; (220.1000) Aberration compensation

---

## References and links

1. M. Schwertner, M. J. Booth, M. A. A. Neil, and T. Wilson, "Measurement of specimen-induced aberrations of biological samples using phase stepping interferometry," *J. Microsc.* **213**(1), 11–19 (2004).
2. M. Schwertner, M. J. Booth, and T. Wilson, "Characterizing specimen induced aberrations for high NA adaptive optical microscopy," *Opt. Express* **12**(26), 6540–6552 (2004).
3. M. Schwertner, M. J. Booth, and T. Wilson, "Specimen-induced distortions in light microscopy," *J. Microsc.* **228**(1), 97–102 (2007).
4. S. W. S. Hell, E. H. K., "Lens Aberrations in Confocal Fluorescence Microscopy," in *Handbook of Biological Confocal Microscopy*, Second ed., J. B. Pawley, ed. (Plenum Press, 1995), pp. 347–354.
5. P. N. Marsh, D. Burns, and J. M. Girkin, "Practical implementation of adaptive optics in multiphoton microscopy," *Opt. Express* **11**(10), 1123–1130 (2003).
6. L. Sherman, J. Y. Ye, O. Albert, and T. B. Norris, "Adaptive correction of depth-induced aberrations in multiphoton scanning microscopy using a deformable mirror," *J. Microsc.* **206**(1), 65–71 (2002).
7. M. Schwertner, M. Booth, T. Tanaka, T. Wilson, and S. Kawata, "Spherical aberration correction system using an adaptive optics deformable mirror," *Opt. Commun.* **263**(2), 147–151 (2006).
8. M. J. Booth, "Wavefront sensorless adaptive optics for large aberrations," *Opt. Lett.* **32**(1), 5–7 (2007).
9. M. J. Booth, M. A. A. Neil, and T. Wilson, "New modal wave-front sensor: application to adaptive confocal fluorescence microscopy and two-photon excitation fluorescence microscopy," *J. Opt. Soc. Am. A* **19**(10), 2112–2120 (2002).
10. M. A. A. Neil, M. J. Booth, and T. Wilson, "New modal wave-front sensor: a theoretical analysis," *J. Opt. Soc. Am. A* **17**(6), 1098–1107 (2000).
11. M. Rueckel, J. A. Mack-Bucher, and W. Denk, "Adaptive wavefront correction in two-photon microscopy using coherence-gated wavefront sensing," *Proc. Natl. Acad. Sci. U.S.A.* **103**(46), 17137–17142 (2006).
12. S. N. S. Reihani, and L. B. Oddershede, "Confocal microscopy of thick specimens," *J. Biomed. Opt.* **14**(3), 030513 (2009).
13. H. Itoh, N. Matsumoto, and T. Inoue, "Spherical aberration correction suitable for a wavefront controller," *Opt. Express* **17**(16), 14367–14373 (2009).
14. N. Devaney, E. Dalimier, T. Farrell, D. Coburn, R. Mackey, D. Mackey, F. Laurent, E. Daly, and C. Dainty, "Correction of ocular and atmospheric wavefronts: a comparison of the performance of various deformable mirrors," *Appl. Opt.* **47**(35), 6550–6562 (2008).
15. C. Paterson, I. Munro, and J. C. Dainty, "A low cost adaptive optics system using a membrane mirror," *Opt. Express* **6**(9), 175–185 (2000).

16. P. Torok, S. J. Hewlett, and P. Varga, "The role of specimen-induced spherical aberration in confocal microscopy," *J. Microsc.* **188**(2), 158–172 (1997).
  17. M. J. Booth, M. A. A. Neil, and T. Wilson, "Aberration correction for confocal imaging in refractive-index-mismatched media," *J. Microsc.* **192**(2), 90–98 (1998).
  18. P. Török, and P. Varga, "Electromagnetic diffraction of light focused through a stratified medium," *Appl. Opt.* **36**(11), 2305–2312 (1997).
  19. P. Török, P. R. T. Munro, and E. E. Kriezis, "High numerical aperture vectorial imaging in coherent optical microscopes," *Opt. Express* **16**(2), 507–523 (2008).
  20. M. Mansuripur, "Effects of High-Numerical-Aperture Focusing on the State of Polarization in Optical and Magneto-optic Data-Storage Systems," *Appl. Opt.* **30**(22), 3154–3162 (1991).
  21. Y. L. Jin, J. Y. Chen, L. Xu, and P. N. Wang, "Refractive index measurement for biomaterial samples by total internal reflection," *Phys. Med. Biol.* **51**(371–N), 379 (2006).
  22. J. C. Lai, Z. H. Li, C. Y. Wang, and A. Z. He, "Experimental measurement of the refractive index of biological tissues by total internal reflection," *Appl. Opt.* **44**(10), 1845–1849 (2005).
  23. M. Schwertner, M. J. Booth, and T. Wilson, "Simulation of specimen-induced aberrations for objects with spherical and cylindrical symmetry," *J. Microsc.* **215**(3), 271–280 (2004).
  24. E. J. Fernandez, L. Vabre, B. Hermann, A. Unterhuber, B. Povazay, and W. Drexler, "Adaptive optics with a magnetic deformable mirror: applications in the human eye," *Opt. Express* **14**(20), 8900–8917 (2006).
  25. S. P. Poland, A. J. Wright, and J. M. Girkin, "Evaluation of fitness parameters used in an iterative approach to aberration correction in optical sectioning microscopy," *Appl. Opt.* **47**(6), 731–736 (2008).
- 

## 1. Introduction

Refractive aberrations impose major limitations on the ability of an optical sectioning microscope, such as a confocal or multiphoton microscope, to produce high quality images at depth in optically thick specimens, by reducing both image resolution and measured intensity. Aberrations arise due to differences between the bulk refractive index of the immersion medium, coverglass and specimen, the inhomogeneous structure of the specimen being imaged [1–3] and from the optical elements of the microscope itself. It has been noted that spherical aberration, caused by refractive index mismatch, is the major source of the reduction in fluorescent signal with focus depth commonly noted by most practicing confocal microscopists [4]. Adaptive optic (AO) techniques have been used successfully in confocal and multiphoton microscopes to correct the wavefront of the incident and emitted light and improve imaging capabilities. In particular, researchers have demonstrated the effectiveness of using a deformable mirror to correct depth induced-aberrations in multiphoton microscopy [5,6] and more generally to correct for first order spherical aberration [7]. In many cases optimization of the acquired image is used to provide feedback to the adaptive correcting element [8], however wavefront sensing methods have also been used [9–11]. The effectiveness of all these approaches is limited both by knowledge about the wavefront aberration and by the ability of the correcting element to generate the required wavefront. Other strategies for reducing spherical aberration include optimizing the refractive index of the immersion medium and changing the effective tube length of the microscope [12]; however AO offers the potential of fast, dynamic wavefront correction to improve image resolution and extend imaging depth for a variety of different imaging configurations.

Wavefront control in optical sectioning microscopy can be achieved using either a deformable mirror (DM) or spatial light modulator (SLM). DMs are capable of fast, wavelength independent wavefront correction and have a high light-utilization efficiency, however as they are typically comprised of a relatively small number of actuators they can be unsuitable for correction of wavefronts with significant high spatial frequency components. SLMs typically contain many thousands of pixel elements that can be controlled to produce high spatial frequency monochromatic, linearly polarized wavefronts [13]. Their principal limitation is that they either operate at relatively low frame rates (typically around 60 Hz for nematic liquid crystal on silicon SLMs), or offer relatively low diffraction efficiencies (ferroelectric liquid crystal SLMs). In the case of either DMs or SLMs the adaptive element is positioned in a plane conjugate to the exit pupil of the microscope objective using afocal relay optics which also magnify the exit pupil of the objective to match the mirror pupil. In this way the adaptive element can be used to precondition the wavefront of the light before it enters the objective and, in a double pass system, also correct the wavefront of the light emitted by the

specimen. For example, in a confocal microscope the illumination beam is focused inside the specimen and the emitted light is then brought to a focus at the detector pinhole.

In this paper we discuss the wavefront aberrations arising in an optical sectioning microscope, with a simple geometrical optics model to describe the effect of a planar refractive index mismatch between the immersion fluid and the specimen and also briefly review the types of aberrations which are introduced by the inhomogeneity of the sample itself. We then present measurements of the influence matrices of two different deformable mirrors and assess their ability to generate the wavefronts determined in the previous section, using a method similar to that employed by other authors to assess the ability of deformable mirrors to generate the ocular and atmospheric wavefront aberrations which arise in retinal and astronomical imaging respectively [14–16]. Finally we present measurements of the linearity and hysteresis of the mirror actuators.

## **2. Wavefront aberrations in optical sectioning microscopy**

In a laser scanning confocal microscope (LSCM) or a scanning multiphoton fluorescence microscope the objective lens focuses light down to a spot within the specimen. Light emitted by the specimen is then collected by the objective and passed to a detector, in the case of a confocal microscope the detector is mounted behind a pinhole positioned in a plane conjugate to the focal plane in the specimen. A two-dimensional (2D) or three-dimensional (3D) image is then built up by scanning the light spot through appropriate regions of the specimen. The resolution of the microscope is strongly dependent on the size of the light spot formed within the specimen and also, in the confocal case, the size of the light spot on the detector pinhole. In general, wavefront aberrations increase the size of the light spot and degrade the resolution of the microscope.

The problem of determining the focal plane irradiance distribution when light is focused through one or more media of differing refractive index has been treated in the context of both optical microscopy [16], photolithography and optical data storage and retrieval. Booth et. al. [17] calculated the wavefront aberration in the exit pupil of the objective using a scalar approach with geometrical considerations and investigated the effect of correcting various aberration terms on the imaging properties of a confocal microscope. More recently Itoh et. al. [13] calculated the wavefront aberration using ray tracing. Török et. al. [18] compared techniques for calculating aberrations due to refractive index boundaries in confocal microscopy and presented expressions for the electric field components when light is focused through a stratified medium. Török et. al. [19] have also addressed the problem of coherent imaging with scattered light in an optical microscope using vector diffraction theory. The importance of including polarization effects increases with the numerical aperture (NA) of the objective and for high NAs a rigorous calculation of the focal plane intensity requires the use of vector diffraction theory. Mansuripur [20] investigated the focal plane intensity as a function of polarization state when focusing through a refractive index boundary with a high NA lens for applications in magneto-optical data storage.

In terms of geometrical optics, the presence of a refractive index mismatch between the objective lens and the image plane means that light rays passing through different parts of the lens pupil are refracted through different angles at the interface; if the immersion medium has a higher refractive index than the specimen, paraxial rays are focused deeper into the specimen than marginal rays (see Fig. 1). This results in an increase in the spatial extent of the irradiance distribution at the Gaussian image plane and a shift in the axial position at which the size of the image is a minimum (circle of least confusion). In general these effects increase with the NA of the objective lens, the magnitude of the refractive index mismatch and the distance between the Gaussian image plane and the refractive index boundary.

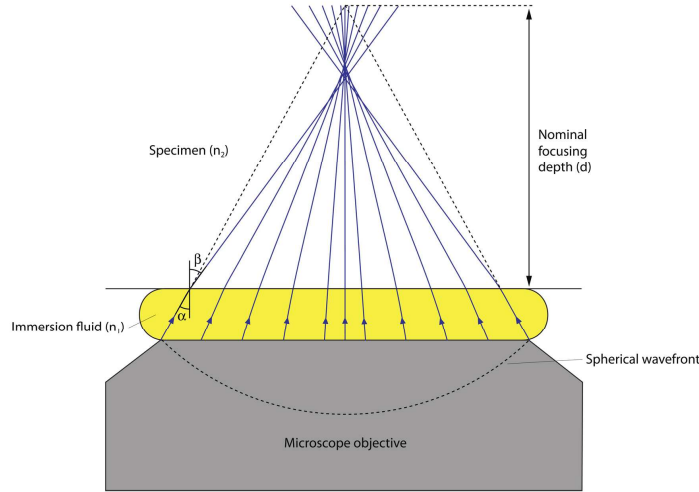


Fig. 1. Schematic diagram showing a high NA objective lens focusing light through a refractive index boundary for the case where the immersion fluid ( $n_1$ ) has a higher refractive index than the specimen ( $n_2$ ).

To calculate the aberration function in the lens pupil we assume a circularly symmetric system with a single planar refractive index mismatch, corresponding to the objective immersion fluid (air, water or oil) and the specimen. In many practical cases the specimen is viewed through a coverglass, however, objective lenses are often designed with this in mind and incorporate an appropriate correction to remove the wavefront aberration resulting from refraction at the interface between the immersion medium and coverglass. In this case the wavefront in the exit pupil of the objective,  $\varphi$ , is given by Eq. (1) [17], where  $d$  is the depth of the nominal focal plane (in the absence of a refractive index boundary),  $\rho$  is the normalized pupil radius and  $\alpha$  and  $\beta$  are the angles of the marginal ray in the first and second media respectively (i.e.  $\text{NA} = n_1 \sin(\alpha)$ ) with respect to the optic axis.

$$\varphi(d, \rho) = \left\{ \sqrt{\text{cosec}^2(\beta) - \rho^2} - \sqrt{\text{cosec}^2(\alpha) - \rho^2} \right\} dn_1 \sin(\alpha) \quad (1)$$

The symmetry of the optical system means that the aberration function can be decomposed into a series of Zernike polynomials of zero azimuthal order  $Z_n^0(\rho)$  with coefficients  $A_{n0}$  (Eq. (2)).

$$\varphi(d, \rho) = \left[ A_{00} + \sum_{n=2}^{\infty} A_{n0} Z_n^0(\rho) \right] dn_1 \sin(\alpha) \quad (2)$$

These polynomials correspond to piston, defocus and spherical aberration terms of increasing radial order, given by Eq. (3).

$$Z_n^0(\rho) = \sqrt{n+1} \sum_{s=0}^{n/2} \frac{(-1)^s (n-2)!}{s!(n/2-s)!} \rho^{n-2s} \quad (3)$$

It can be shown [17] that in this case the Zernike coefficients can be calculated using Eqs. (4) and (5).

$$A_{n0} = B_n(\alpha) - B_n(\beta) \quad (4)$$

$$B_n(\gamma) = \left[ 1 - \left( \frac{n-1}{n+3} \right) \tan^4(\gamma/2) \right] \frac{\tan^{n-1}(\gamma/2)}{2(n-1)\sqrt{n+1}} \quad (5)$$

From Eq. (1) the amplitude of the aberration increases with NA, focusing depth and the magnitude of the refractive index mismatch.

Using this model we have calculated the wavefront in the exit pupil of the objective lens for the three different imaging conditions given in Table 1. The NA and working distance values all correspond to commercially available objective lenses; 1.518 is the refractive index of a standard microscope immersion oil at the 546.1 nm mercury emission line. For the highest NA objective some of the outer rays will be totally internally reflected at the boundary between the immersion medium and the specimen and hence will not contribute to the image formed in the specimen. The refractive index of biological tissue at visible wavelengths is generally between that of water and immersion oil, with other authors [21,22] finding values of between 1.35 and 1.48 at 532 nm and 633 nm for some typical biological materials. We choose water as the specimen medium to illustrate the types of wavefront aberrations which can arise in optical sectioning microscopy and to provide a scheme against which to test the capabilities of the two DMs. In practical situations in which the refractive index mismatch between immersion medium and specimen is smaller, the amplitude of the wavefront aberration will be reduced and the DMs should allow even better wavefront correction and the extension of diffraction limited imaging to greater penetration depths. In practice the effects of spherical aberration can be reduced significantly by using a water, rather than oil, immersion objective when imaging specimens with a refractive index close to that of water at depths of greater than a few  $\mu\text{m}$ .

**Table 1. - Three imaging conditions used to test DMs**

NA	Immersion medium	Specimen medium	Maximum focusing depth (working distance)
1.35	Oil ( $n_1 = 1.518$ )	Water ( $n_2 = 1.33$ )	150 $\mu\text{m}$
1.2	Oil ( $n_1 = 1.518$ )	Water ( $n_2 = 1.33$ )	150 $\mu\text{m}$
0.75	Air ( $n_1 = 1.00$ )	Water ( $n_2 = 1.33$ )	600 $\mu\text{m}$

The calculated wavefront in the exit pupil for each case is shown in Fig. 2 below, for each imaging condition the wavefront is shown before (dashed line) and after (solid line) subtraction of the defocus term ( $Z_2^0$ ) from the aberration function. Note that the amplitude of the wavefront aberration is largest close to the edge of the pupil and that the overall wavefront deviation from flatness increases with the NA (from Eq. (1) it is also apparent that the amplitude of the wavefront aberration also increases linearly with focusing depth).

The model described above approximates the specimen as a homogenous medium of uniform refractive index. Clearly, real biological samples are far from homogenous and as a result the wavefront aberration will vary as the focal spot is scanned through the specimen. A detailed investigation of specimen induced aberrations is beyond the scope of this paper, however other authors have quantified the typical aberrations arising in high NA microscopy of biological samples using interferometric measurements in terms of Zernike modes [2] and have also simulated specimen induced aberrations for simple objects [23]. These results indicate that the amplitude of these aberrations tends to increase with the NA and that correction of low order Zernike modes (up to and including term 22) can significantly improve imaging.

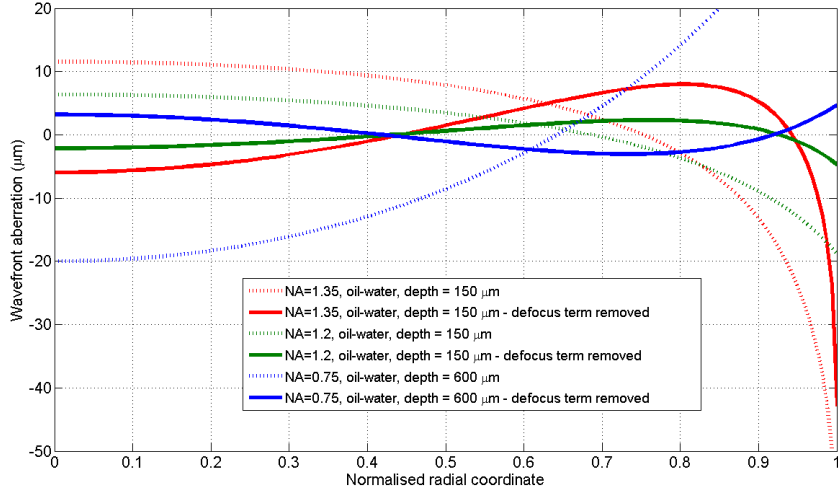


Fig. 2. Calculated wavefront in the exit pupil of the objective lens for three different sets of imaging parameters. Dashed lines show the total wavefront aberration, solid lines show the wavefront with the defocus term removed.

### 3. Characterisation of Deformable Mirrors

Deformable mirrors offer a way of controlling the wavefront of the light in an optical sectioning microscope and compensating for aberrations. We looked at two different deformable mirrors for this purpose: a Mirao 52-e electromagnetic actuator mirror with a 15 mm diameter pupil produced by Imagine Eyes and a piezoelectric deformable mirror (PDM) with a 50 mm diameter pupil from Flexible Optical B.V. The first device comprises a protected silver coated flexible membrane with 52 electromagnetic actuators arranged on a square grid pattern with an interactor spacing of 2.5 mm. The manufacturer specifies the stroke of the Mirao 52-e in terms of the maximum peak to valley amplitude of the various Zernike modes it can generate; for wavefront tilt this is 50  $\mu\text{m}$  across the pupil. Previous authors have described use of this DM for ocular aberration correction [24]. The second DM has a deformable plate with a free edge, coated with aluminium and a protective layer of fused silica, bonded to 37 piezoelectric actuators also arranged on a square grid with an actuator pitch of 6.83 mm and a maximum free actuator stroke of 8  $\mu\text{m}$ . Each mirror is controlled using a PC which allows sets of actuator voltage commands to be sent to the device, via a high voltage amplifier in the case of the PDM and via a voltage to current converter for the Mirao 52-e.

#### 3.1 Spatial Modes of the Mirrors

Assuming a linear response the mirror deformation,  $\varphi_m$ , for a given set of actuator signals,  $x_m$ , is given by:

$$\varphi_m = A_m x_m \quad (6)$$

Where  $A_m$  is the influence matrix of the mirror. The actuator signals which give the best fit to a given target wavefront  $\varphi_0$ , can then be calculated by premultiplying  $\varphi_0$  by the pseudo inverse of the influence matrix which itself can be found from a singular value decomposition of  $A_m$ .

$$\begin{aligned} A_m &= USV^T \\ A_m^{-1} &= VS^{-1}U^T \end{aligned} \quad (7)$$

The columns of the  $U$  matrix comprise a set of  $N$  orthogonal spatial modes of the mirror (where  $N$  is the number of mirror actuators) and the diagonal elements of  $S$  represent the gain

of each mode, the columns of  $V$  make up an orthogonal set of actuator signals. A smaller gain means that a large actuator signal is required to produce a given amount of that mode. The spatial modes included in the wavefront expansion can be altered by setting the relevant diagonal elements of  $S$  to zero or by conditioning the  $U$  matrix. To restrict the expansion to the first  $n$  ( $<N$ ) spatial modes, elements of columns  $n + 1$  to  $N$  of  $U$  are set to zero.

Once the influence matrix and its inverse are known, the ability of the mirror to produce a given wavefront aberration ( $\varphi_0$ ) can be determined from.

$$\varphi_m = USV^T f(VS^{-1}U^T \varphi_0) \quad (8)$$

Where  $f$  is a clipping function to account for the limited stroke of the mirror actuators and is defined by

$$f = \begin{cases} x_i & \text{for } |x_i| \leq x_{\max} \\ x_{\max} \frac{x_i}{|x_i|} & \text{for } |x_i| \geq x_{\max} \end{cases} \quad (9)$$

Influence matrices for both mirrors were measured using a phase stepping Fizeau interferometer (Zygo corporation) with the data acquisition and fringe analysis carried out using MetroPro 7.3.2 software. For both mirrors, the same voltage signal was applied to each mirror actuator in turn and an interferogram was recorded. The signal size was chosen to provide a significant actuator displacement without exceeding the dynamic range of the interferometer; for the PDM this signal corresponded to 20% of the maximum positive voltage and for the Mirao 52-e to 5%. The initial shape (the surface figure of the mirror with zero volts applied to all actuators) of both mirrors was significantly non-planar and in order to reduce the number of interference fringes, and increase both the available dynamic range of the interferometer and reduce measurement uncertainties, actuator influence functions were measured relative to a partially flattened mirror shape. The Mirao 52-e was flattened by applying a flat mirror signal matrix supplied by the manufacturer and the PDM was flattened by applying an actuator signal matrix approximately to correct for 1  $\mu\text{m}$  of defocus calculated by solving a biharmonic equation relating mirror displacement to the stiffness of the deformable plate and the applied load. This flattening reduces the stroke of the actuators available to generate the required wavefront, however for the Mirao 52-e the signal matrix required to flatten the mirror used no more than 7% of the maximum signal for any given actuator. The initial shape of the PDM is dominated by a defocus term which can be readily compensated through introducing an equal and opposite amount of defocus into the wavefront incident on the mirror by displacing it away from the plane conjugate with the exit pupil of the objective. For these reasons, in the following analysis we ignore the reduction in stroke of the mirrors caused by their initial shapes.

To measure the influence function of a given actuator the mirror was flattened and an interferogram was recorded before a signal was applied to the actuator under test and a second interferogram recorded; the difference between the two interferograms then indicates the influence function of that actuator. Due to the double pass effect, the amplitude of the mirror deformation is equal to half that of the measured wavefront. To build up the full mirror influence matrix this sequence was then repeated for all other actuators. In order to reduce the effects of hysteresis, before flattening the minimum possible signal was applied to all of the mirror actuators.

The finite signal which can be applied to a given actuator means that the optimum mirror shape for a given target wavefront is not necessarily achieved using all of the mirror modes. In particular, orthogonal modes with higher spatial frequency content tend to be associated with smaller singular values; this means that a larger signal in the actuator signal space is required to produce a given amplitude of one of these modes compared with modes of lower spatial frequency content. Including spatial modes with small singular values in the mirror control matrix can therefore lead to actuator clipping which can have a significant effect on the mirror shape. For the Mirao 52-e the voltage signal sent to each actuator must be within the range  $-1$

V to + 1 V. An additional constraint, due to the mirror drive unit provided by the manufacturer, is that the sum of the magnitudes of the signals supplied to all actuators must be less than 25V. To account for this if the sum of the actuator signal magnitudes exceeded 25V they were all scaled down after truncation of actuator voltages.

In order to determine both the optimum mirror pupil diameter and the optimum number of mirror spatial modes to use in the wavefront expansion, we simulated the residual wavefront error in the mirror fit to the wavefront for an NA = 1.2 oil immersion objective focusing 100  $\mu\text{m}$  into water, with the defocus term removed. This wavefront has a root mean square (rms) deviation from flatness of 1.10  $\mu\text{m}$ . Figure 3 and Fig. 4 show the effect of varying both mirror aperture ratio and the number of spatial modes used in the wavefront expansion on the rms of the residual wavefront error for the PDM and Mirao 52-e mirrors respectively.

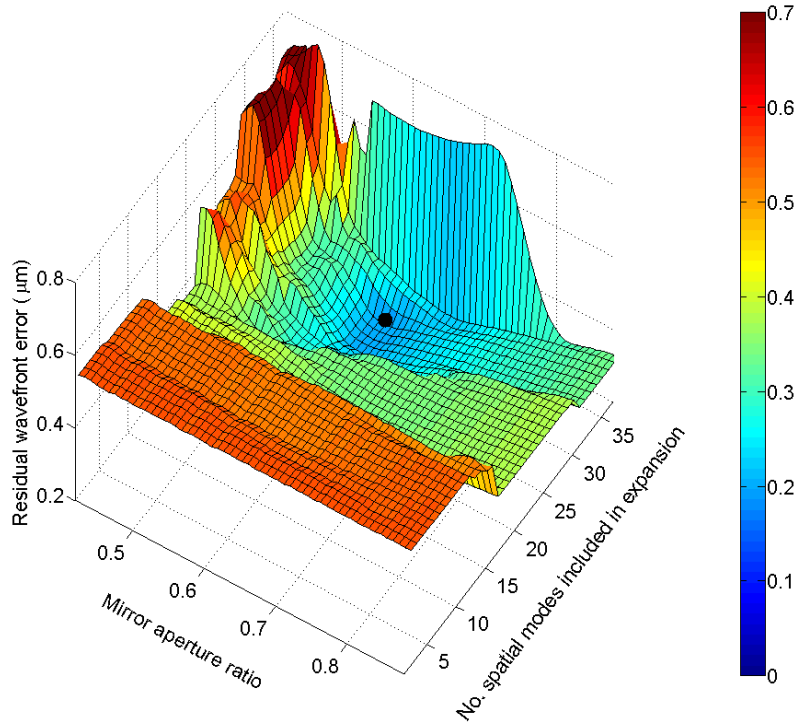


Fig. 3. Surface plot showing the residual error in a fit of the PDM to the wavefront arising from an NA = 1.2 oil immersion objective focusing 100  $\mu\text{m}$  into water. In this case the minimum residual wavefront error is 0.20  $\mu\text{m}$ , which occurs for an aperture ratio of 0.59 using 33 of the 37 available spatial modes (shown by the filled black circle).

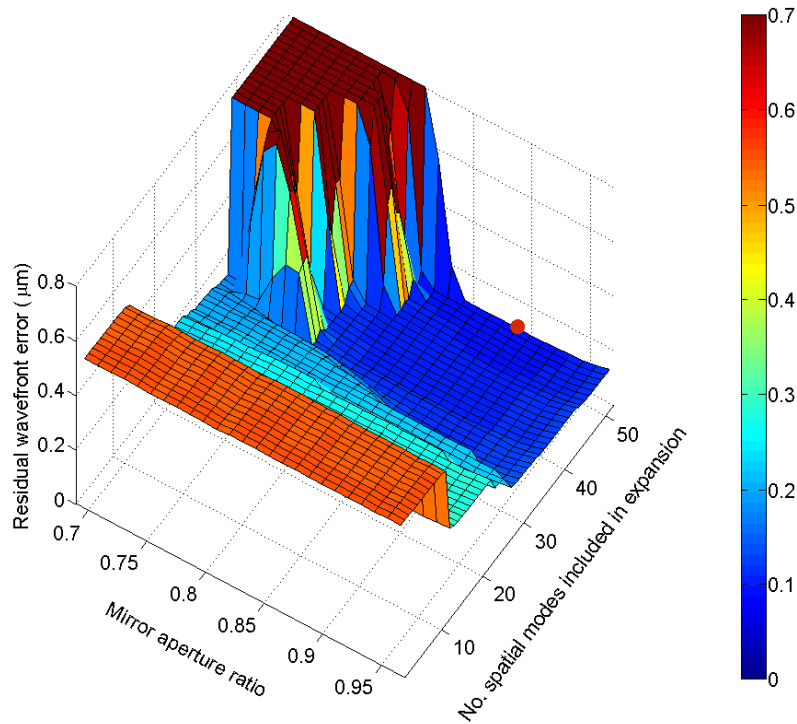


Fig. 4. Surface plot showing the residual error in a fit of the Mirao 52-e to the wavefront arising from an NA = 1.2 oil immersion objective focusing 100  $\mu\text{m}$  into water. In this case the minimum residual wavefront error is 0.09  $\mu\text{m}$ , which occurs for an aperture ratio of 0.89 using all 52 of the spatial modes (shown by the filled red circle).

For the PDM the optimum fit to the simulated wavefront leaves an rms residual wavefront error of 0.20  $\mu\text{m}$  and occurs for a mirror aperture ratio of 0.59 using 33 of the 37 spatial modes. As can be seen in Fig. 5, which shows the actuator layout for both mirrors, the optimum aperture ratio for the PDM corresponds to the case where a ring of actuators lie outside the illuminated pupil of the mirror. The large residual error in the fit using all 37 spatial modes is a result of mode 37 having a small singular value, which results in significant actuator clipping when the mode is included in the expansion. For the Mirao 52-e a good fit to the simulated wavefront is achieved using most of the available spatial modes and a large mirror aperture ratio, with a minimum rms residual wavefront error of 0.09  $\mu\text{m}$  for an aperture ratio of 0.89. Close to the minimum, the residual wavefront error is fairly insensitive to both the aperture ratio and the number of spatial modes included in the expansion, in the latter case indicating that inclusion of the higher order modes does not substantially improve the fit. A large aperture ratio is favoured for this DM as a ring of actuators are outside the maximum useable pupil of the mirror (Fig. 5) which is limited by the manufacturer using an aperture fitted to the front of the mirror. For smaller aperture ratios a better correction is achieved by including fewer spatial modes in the wavefront expansion as the effect of aperture clipping is reduced.

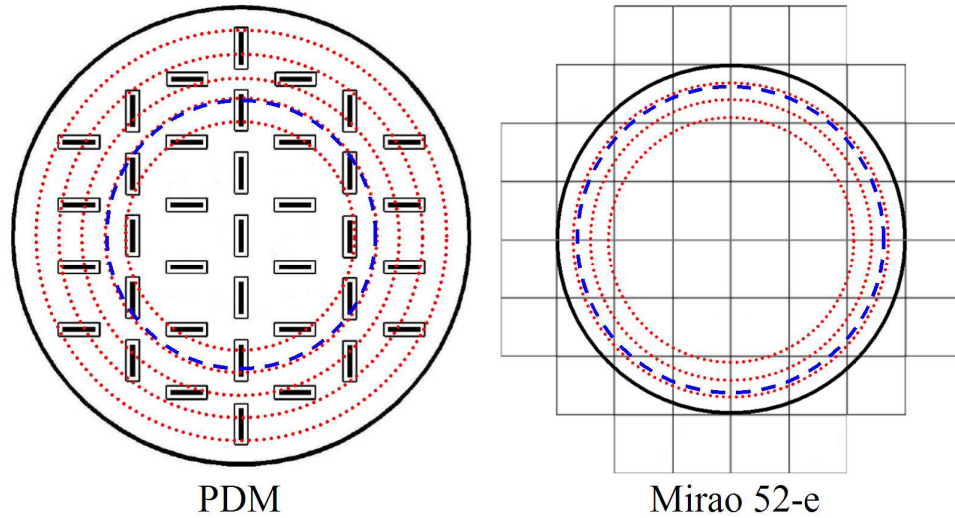


Fig. 5. Actuator layout in relation to the mirror pupil for the PDM (left) and the Mirao 52-e (right). PDM actuators indicated by black rectangles with white borders, Mirao 52-e actuators indicated by square cells. For each mirror the full useable aperture is indicated by the solid black line, reduced apertures in steps of 10% are indicated by the dotted red lines, the dashed blue line indicates the optimum pupil size for correction of the aberrated wavefront resulting from an NA = 1.2 oil immersion objective focusing 100  $\mu\text{m}$  into water.

Figure 6 shows phase maps for the calculated wavefront for an NA = 1.2 oil immersion lens focusing 100  $\mu\text{m}$  into water along with the best fit mirror surface and the residual wavefront error using the optimized aperture ratio and number of spatial modes in the expansion. The largest differences occur at the edge of the pupil where the wavefront aberration has the greatest amplitude. The rings apparent in the residual wavefront error for the Mirao 52-e are an artifact of the measurement of the actuator influence functions. It should be noted that an alternative way of dealing with actuator clipping or an optimization type approach to determine actuator signals such as using a genetic algorithm [25] may lead to a closer fit between the mirror to the required wavefront and therefore a better aberration correction, however such an investigation is beyond the scope of this paper.

Figure 7 and Fig. 8 show the Strehl ratio at a wavelength of 633 nm for the image of the light spot formed in the specimen at different depths with and without aberration correction for the three imaging conditions described in Table 1 using both deformable mirrors. The Strehl ratio was calculated using the exponential Maréchal approximation given in Eq. (10), where  $\sigma$  is the rms wavefront error in wavelengths.

$$S(\sigma) \approx e^{-(2\pi\sigma)^2} \quad (10)$$

In this case the Strehl ratio describes the imaging in the illumination path of the microscope only. In an episcopic confocal system where the illumination light is scattered from the specimen and passes back through the interface between the specimen and immersion medium, the wavefront aberration is doubled along with the residual wavefront error reducing the Strehl ratio from  $S$  to  $S^4$ . For each different imaging condition we fix the mirror aperture ratio, at 0.59 for the PDM and 0.87 for the Mirao 52-e, and determine the optimum wavefront correction which each mirror can achieve as a function of depth, optimizing the number of spatial modes used in the expansion at each depth. Fixing the aperture ratio is a practical restriction as it is unlikely to be feasible to arbitrarily change the magnification of the relay optics for different focusing depths. For a Strehl ratio of 0.8 or greater, imaging is generally considered to be diffraction limited.

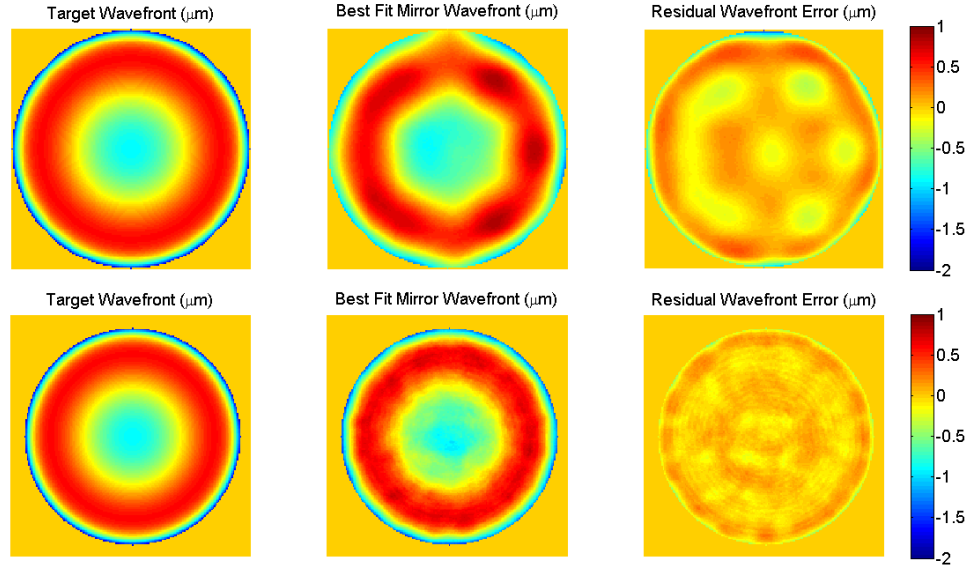


Fig. 6. The ability of both DMs to fit the simulated wavefront for an NA = 1.2 oil immersion objective imaging 100  $\mu\text{m}$  into water with optimized aperture ratio and number of spatial modes. Top - PDM with an aperture ratio of 0.59, 33 spatial modes (rms residual wavefront error of 0.20  $\mu\text{m}$ ). Bottom - Mirao 52-e with an aperture ratio of 0.89 and 52 spatial modes (rms residual wavefront error of 0.09  $\mu\text{m}$ ).

Both DMs offer a substantial improvement in imaging for the NA = 1.2 and NA = 0.75 cases, as summarised in Table 2. The large amplitude of the wavefront aberration at the edge of the pupil for the NA = 1.35 oil immersion objective means that neither DM is able to fit the required wavefront effectively for focusing depths of greater than a few  $\mu\text{m}$ . Due to its larger actuator stroke the Mirao 52-e is able to maintain diffraction limited imaging to greater depth than the PDM. For the NA = 1.2 oil immersion objective, aberration correction using the Mirao 52-e can extend diffraction limited imaging from a depth of 4  $\mu\text{m}$  to over 50  $\mu\text{m}$  and using the PDM to 26  $\mu\text{m}$ . For the NA = 0.75 objective the increase in diffraction limited depth penetration is from 14  $\mu\text{m}$  to 280  $\mu\text{m}$  for the PDM and the Mirao 52-e respectively. Doubling the size of the residual wavefront error to simulate correction in both the illumination and detection paths, without correction diffraction limited imaging is possible to a depth of 2  $\mu\text{m}$  and 7  $\mu\text{m}$  using the NA = 1.2 and NA = 0.75 objective respectively. Using the PDM this increases to 14  $\mu\text{m}$  and 66  $\mu\text{m}$  and using the Mirao 52-e to 25  $\mu\text{m}$  and 140  $\mu\text{m}$  for the NA = 1.2 and NA = 0.75 objectives respectively.

Table 2. Increase in maximum focusing depth at which diffraction limited is possible after aberration correction using both DMs

		Maximum focusing depth for diffraction limited imaging, Strehl ratio $\geq 0.8$ ( $\mu\text{m}$ )		
		No correction	PDM	Mirao 52-e
Illumination only	NA = 1.2 (oil-water)	4	26	50
	NA = 0.75 (air-water)	14	120	280
Illumination and detection	NA = 1.2 (oil-water)	2	14	25
	NA = 0.75 (air-water)	7	66	140

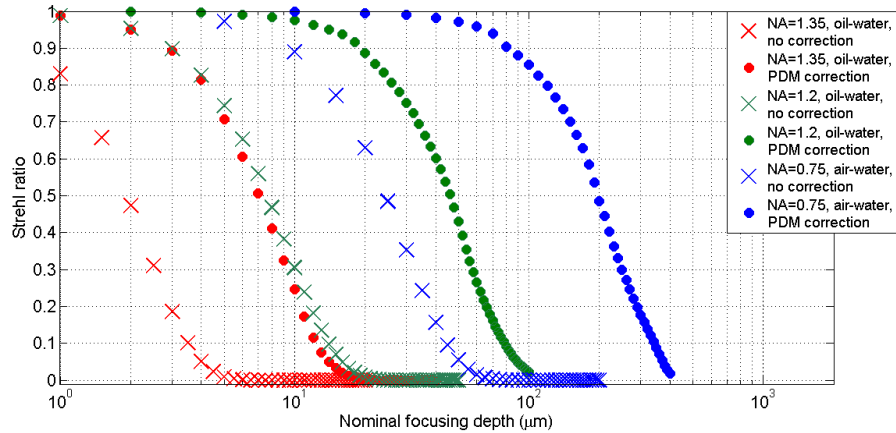


Fig. 7. Strehl ratio as a function of focusing depth with and without aberration correction using PDM with an aperture ratio of 0.59 and optimised number of spatial modes at each depth.

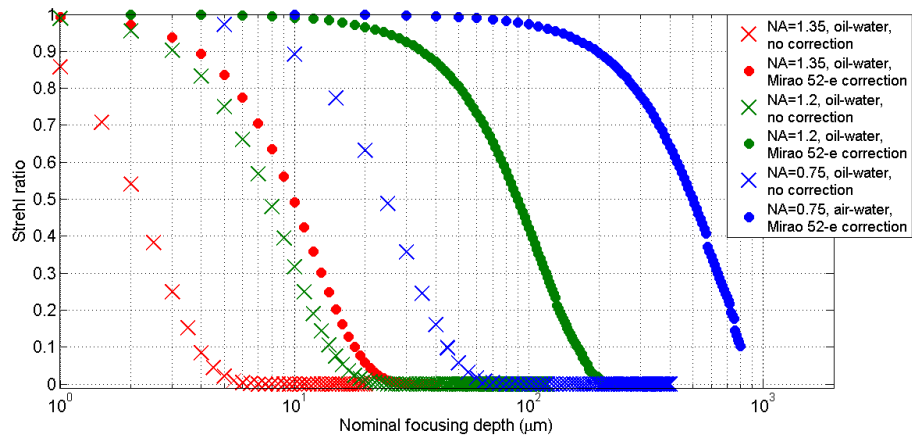


Fig. 8. Strehl ratio as a function of focusing depth with and without aberration correction using Mirao 52-e with an aperture ratio of 0.89 and optimised number of spatial modes at each depth.

### 3.2 Linearity and hysteresis of mirror actuators

The preceding analysis assumes that the mirror influence matrix has a linear response with applied actuator signal, i.e. that  $A_m$  in Eq. (6) is independent of  $x_m$  and the deformation of the mirror deformation,  $\varphi_m$ , obeys Eq. (11) for all permitted combinations of actuator signals  $x_1$  and  $x_2$ .

$$\varphi_m(x_1) + \varphi_m(x_2) = \varphi_m(x_1 + x_2) \quad (11)$$

Any deviation from linearity affects the range of deformations which the mirror can actually produce. Furthermore, non-linearity and hysteresis affect the ability of the DM to be used in an open loop system and the speed of correction which is achievable in a closed loop configuration. We assessed the displacement linearity of individual DM actuators by measuring the influence functions of three actuators as a function of supplied voltage using a Shack-Hartmann wavefront sensor (SHS). The mirror pupil was illuminated by the collimated output from a 635 nm laser diode, with the DM tilted slightly to separate the incident and reflected beams. The reflected light passed through a pair of doublet lenses and onto the SHS, with the doublet lenses serving to conjugate the mirror pupil with the lenslet array of the SHS

and demagnify the image of the mirror pupil and underfill the sensor. The linearity of the SHS for measurement of spherical wavefronts had been previously assessed by translating a point source along an optical rail in known distance increments and found to be better than 1.5% for a radius of curvature of between 170 mm and 1500 mm, equivalent to peak to valley Zernike defocus terms of between 23  $\mu\text{m}$  and 2  $\mu\text{m}$ .

For each DM the response of three actuators across the pupil was measured over the full range of actuator input signals. Figure 9 shows the measured peak to valley deviation across the mirror pupil as each of these actuators is driven in 0.1V increments from 0V to +1V, back down through 0V to -1V and back to +0.2V. Hysteresis is quantified using a hysteresis parameter defined as the ratio of the largest difference in measured mirror displacement at any input to the total measured displacement range. As expected, since it uses piezoelectric actuators, the PDM exhibits significant hysteresis with a mean measured hysteresis parameter across the three actuators of 12.3%, the Mirao 52-e shows only 0.8% hysteresis which is not significant considering the uncertainties in the actuator displacement measurements. For both mirrors these values are in good agreement with specifications provided by the manufacturers.

Although it exhibits significant hysteresis, the PDM behaves linearly provided the actuator voltage is changed in the same direction (either increasing or decreasing), and a sufficiently large voltage difference is applied after any change in direction. For example, after driving the actuators to -1.0V their average response from -0.6V to +1.0V can be fitted with a linear trend line which has a mean correlation coefficient of 0.9995; in the opposite direction, from +0.6V to -1.0V, the mean correlation coefficient is 0.9986. The Mirao 52-e exhibits good linearity of response with a mean correlation coefficient of 0.9994 over the three measured actuators. Slight deviations from linearity are apparent when the actuators are driven close to the minimum and maximum voltages, which could be attributable to a non-linear response in the SHS for very large spot deviations in the Hartmanngram. The effect is sufficiently small as not to significantly affect the previous analysis.

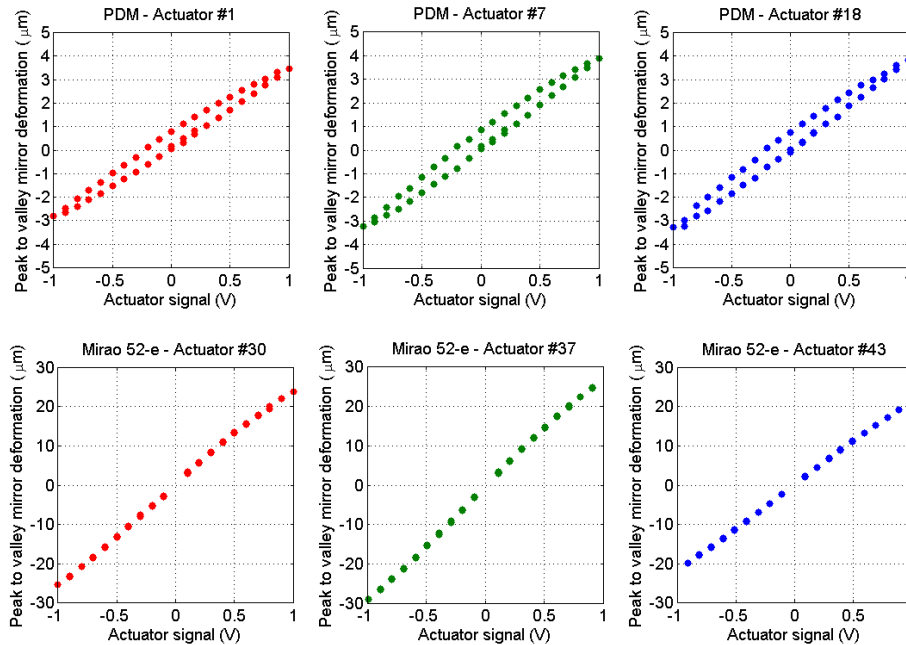


Fig. 9. Peak to valley displacement of both PDM (top) and Mirao 52-e (bottom) mirrors as individual actuators are driven.

A further assumption of the linear model of mirror behaviour which we have adopted is that there is no significant cross talk or coupling between the mirror actuators. To test whether this is the case we used a Fizeau interferometer to measure the mirror surface when different

combinations of actuators are activated simultaneously and compared the resulting deformation with that expected from a linear superposition of individual actuator influence functions. For each DM we looked at four adjacent actuators near the centre of the mirror pupil and four adjacent actuators close to the edge of the pupil, in each case measuring the mirror deformation when 2, 3 and all 4 actuators are activated at the same signal level as used previously to measure the influence functions. For both DMs the observed differences between the measured wavefronts and the linear superposition of influence functions were not significantly greater than the measurement repeatability. This suggests that for relatively small actuator displacements, our simple linear uncoupled model of the mirror behaviour is a good approximation.

#### **4. Conclusions**

We have characterized two deformable mirrors, a piezoelectric mirror from Flexible Optical B.V. and a Mirao 52-e electromagnetic mirror from Imagine Eyes, for use in correcting the wavefront aberrations that arise in an optical sectioning microscope due to a refractive index mismatch between the immersion medium and the specimen. By projecting the measured spatial modes of the mirror on to simulated wavefront aberrations arising for three different imaging conditions we have demonstrated that both mirrors can substantially reduce the wavefront aberration in the exit pupil of the microscope objective and increase the depth at which diffraction limited images may be acquired. Our results are also applicable for the use of DMs in other systems where a high NA objective lens is used to produce a focused light spot at depth through a refractive index mismatch, such as laser micromachining, high density optical data storage and optical tweezers.

#### **Acknowledgements**

This work was funded by the National Measurement System Directorate of the UK Department for Innovation, Universities and Skills. The identification of certain commercial equipment does not imply recommendation or endorsement by NPL, nor does it imply that the equipment identified is the best available for the purpose.